Journal of Marine Research, 63, 1017–1039, 2005

The variability of the East Sakhalin Current induced by winds over the continental shelf and slope

by Genta Mizuta[1], Kay I. Ohshima[2], Yasushi Fukamachi[2] and Masaaki Wakatsuchi[2]

ABSTRACT

Long-term current measurements of the East Sakhalin Current (ESC) in the Sea of Okhotsk are analyzed using the technique of empirical orthogonal functions (EOFs) in the frequency domain. The first and second EOFs at subtidal frequencies represent motions over the continental shelf and slope, respectively, corresponding to the variability of the two cores of the intense ESC. The first EOF can be explained by the first-mode coastal trapped wave (CTW). The structure of the second EOF is similar to that of the second-mode CTW to the first approximation. According to the distribution of the cross-spectra between EOFs and the wind stress over the whole area of the Sea of Okhotsk, the first EOF is correlated with the alongshore component of the wind stress over the northern and western shelves. The distribution of the phase of the wind stress, which is correlated with the first EOF, indicates that a resonance between the CTW and wind stress drives the motion represented by the first EOF at lower frequencies. At higher frequencies the phase of the wind stress correlated with the first EOF is almost uniform in space, being consistent with the greater speed of phase propagation of the EOF compared with that for the free CTW at these frequencies. The second EOF is correlated with the wind stress curl in the central part of the Sea of Okhotsk. The motion by the second EOF is confined over the slope at lower frequencies and becomes large over the shelf at higher frequencies. This change in the structure of the second EOF is consistent with the results of the numerical experiment of the flow induced by the offshore forcing by Chapman and Brink (1987). The phase of the wind stress curl which is correlated with the second EOF changes clearly in space at some frequencies, suggesting that the motion represented by the second EOF propagates along the isobath with the coast to the right. The wind stress curl contains the wavenumber resonant with the lowest two or three modes of CTWs.

1. Introduction

The Sea of Okhotsk is a marginal sea adjacent to the North Pacific (Fig. 1) and the formation region of dense shelf water which is an important source of the ventilation of North Pacific Intermediate Water (Kitani, 1973; Talley, 1991; Yasuda, 1997). The circulation in this sea consists of a northward flow in the eastern part and a southward flow along the western boundary, the East Sakhalin Current (ESC) (Leonov, 1960; Moroshkin,

1. Graduate School of Environmental Earth Science, Hokkaido University, Kita 10 Nishi 5, Sapporo 060-0810, Japan. ***email: mizuta@ees.hokudai.ac.jp***

2. Institute of Low Temperature Science, Hokkaido University, Sapporo, Japan.

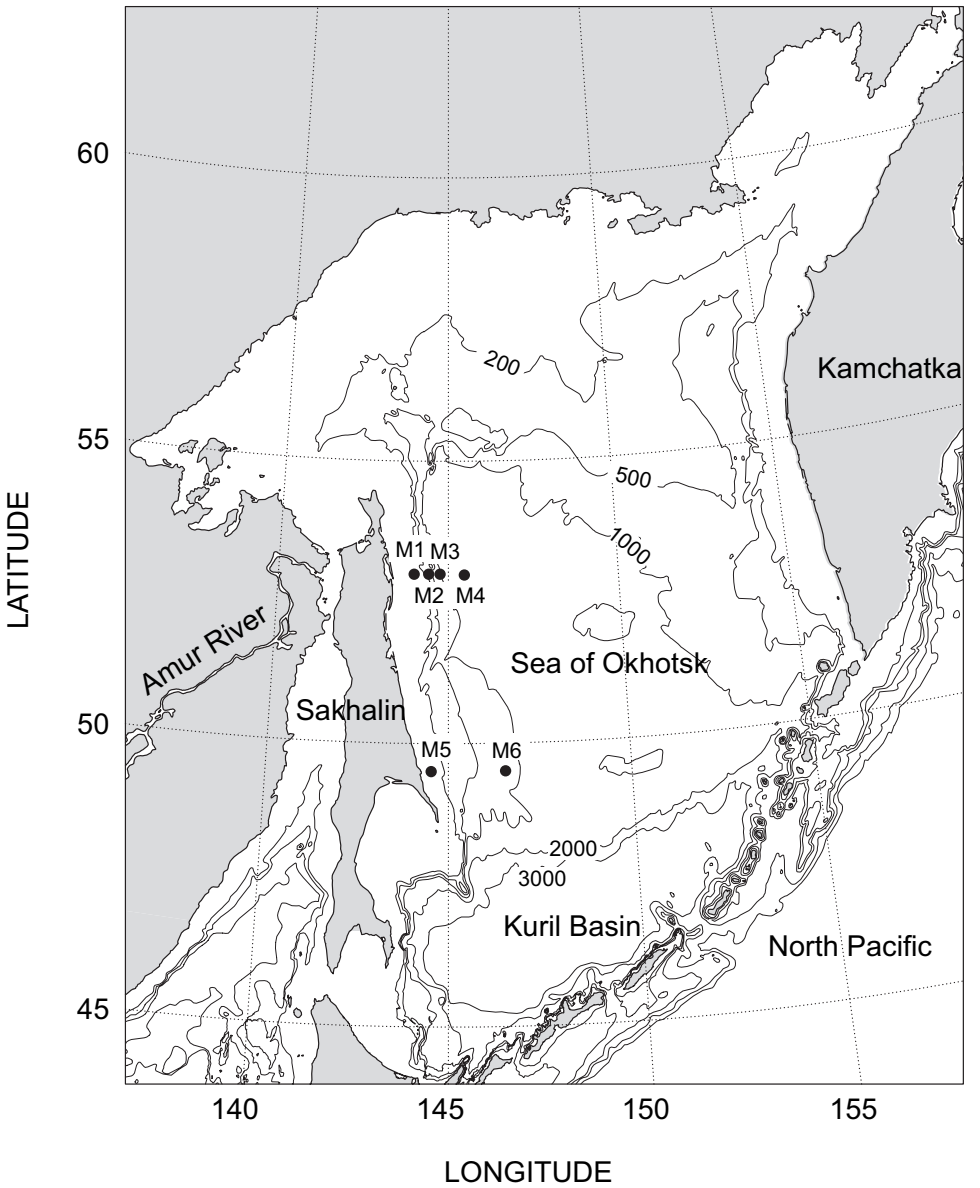

Figure 1. A map with locations of current meter moorings (solid circles). Contours indicate isobaths based on the General Bathymetric Chart of the Ocean (GEBCO).

1966). Dense shelf water (Gladyshev *et al.,* 2003) and sea ice (Parkinson and Grads, 1983; Kimura and Wakatsuchi, 2000) are advected by the ESC. The short-term variability of the ESC is potentially important for the sea ice distribution, which often changes largely in a

few days, and the precise prediction of oil spill from oil fields over the Sakhalin shelf. Bottom topography of the Sea of Okhotsk is characterized by the Kuril Basin deeper than 3000 m in the southern part and a rather shallow region in the central and northern parts. Because of this shallow depth and the large Coriolis parameter with small variation in high latitudes, the topographic beta effect dominates the planetary beta effect in most parts, suggesting stronger control of the circulation by the former effect.

Recent observations in 1998–2000 showed that the ESC is distributed over the continental shelf and slope and extends from the surface to at least depths around 1000 m (Mizuta *et al.,* 2003). The ESC transport varies seasonally with a maximum of 12.3×10^6 m^3 s^{-1} in February, a minimum of 1.2×10^6 m^3 s^{-1} in October, and an annual average of 6.7×10^6 m^3 s^{-1}. Different cores of intense flow exist in the ESC (Ohshima *et al.,* 2002; Mizuta *et al.,* 2003). The first and second cores are centered over the slope and shelf, respectively. Most of the transport of the ESC is maintained by the first core. The geostrophic circulation in the central part of the Sea of Okhotsk is nearly in Sverdrup balance, and the first core of the ESC is arguably the western boundary current of the circulation driven by the wind stress curl (Ohshima *et al.,* 2004). The second core is intensified in fall and associated with less dense water provided by the Amur River discharge (Mizuta *et al.,* 2003). On the other hand, it is shown in both barotropic and continuously stratified models that the alongshore component of the wind stress generates a southward flow over the shelf (Simizu and Ohshima, 2002; Simizu, 2003). Another core that is intensified toward the bottom exists near the northern shelf associated with dense shelf water formed there (Mizuta *et al.,* 2003). This core becomes weak toward the south.

While these works clarified the mean structure and seasonal variability of the ESC, the variability in time scales shorter than a season has not been fully explored. The theory of coastal trapped waves (CTWs) excited by the alongshore wind stress has often been used to explain the short-term variability of alongshore velocity and temperature observed in various coastal areas in the world (e.g. Brink, 1982). On the other hand, Chapman and Brink (1987) studied numerically a flow over the shelf and slope induced by an oscillating forcing in the deep, offshore region in the form of a specified pressure field. They showed that the distribution of the flow changes drastically with the frequency of the forcing. When the frequency of the forcing is higher than about 0.1 cpd, strong resonances of CTWs with the forcing occur to induce a strong flow over the shelf. At lower frequencies, the flow is confined over the slope because the flow over the shelf is dissipated by bottom friction which is strong in shallow regions.

In this study, the short-term variability of velocity in the ESC is examined, using velocity data obtained by moored current measurements off the east coast of Sakhalin as part of a joint Japanese-Russian-U.S. study. Of interest here is whether there is any short-term variability confined in some regions such as that found in the mean flow and what is the driving mechanism of such variability. Coastal trapped and topographic waves are the possible causes of the variability. To examine the structure of such variability, the technique of empirical orthogonal functions (EOFs) in the frequency domain is used

Table 1. Current velocity data used to obtain EOFs. The 6th and 8th column denote the nominal depth at which velocity data were obtained and the area of the segment in the cross sectional area along 53N and 49.5N. See the text for details.

Station	Level	Lat (°N)	Lon (°E)	Bottom depth (m)	Nominal depth (m)	Period	Area (10^6 m^2)
M1	1	53.0	144.0	100	60	98/Jul/28–99/Jul/10	4.4
M2	1	53.0	144.4	480	200	98/Jul/29–99/Sep/06	7.4
	2				430	98/Jul/29–99/Sep/06	3.8
M3	1	53.0	144.8	970	170	98/Jul/29–99/Sep/06	11.2
	2				460	98/Jul/29–99/Sep/06	12.4
	3				870	99/Jan/17–99/Sep/06	17.0
M4	1	53.0	145.5	1720	200	98/Jul/30–99/Sep/02	16.4
	2				480	98/Jul/30–99/Sep/02	63.4
M5	1	49.5	144.5	130	60	98/Aug/02–99/Jul/14	20.9
M6	1	49.5	146.5	790	180	98/Aug/03–99/Sep/03	47.3
	2				480	98/Aug/03–99/May/11	39.9
	3				750	98/Aug/03–99/Sep/03	32.9

(Wallace and Dickinson, 1972). The EOFs obtained with this technique are complex and can express not only the amplitude but also the phase propagation of variability at different sites. Then the relationship between the EOFs and the wind stress and its curl is examined. In Section 2 the current velocity data, and the method we used to obtain the EOFs are described. The structure of the EOFs is examined and compared with that of CTWs in Section 3. Then the relationship between the EOFs and the wind stress is also examined there. Results are summarized with additional discussion in Section 4.

2. Data

Since velocity data over both the continental shelf and slope were obtained simultaneously at two different latitudes, 49.5N and 53N from July 1998 to September 1999, velocity data obtained were analyzed for this period (Fig. 1, Table 1). Details of mooring locations, periods, and instruments are described in Mizuta *et al.* (2003). The two cores of the ESC over the slope and shelf were clear at these mooring sites, while the core associated with dense shelf water was weak. At each mooring site, current meters and ADCPs were moored at water depths around 200 and 450 m and/or near the bottom. The vertical resolution of velocity data was 4 or 8 m at depths where ADCP data were available and 200 to 400 m at other depths. To eliminate the difference of the vertical resolution with instruments only one depth bin for each ADCP was used. Velocity data used to obtain EOFs are listed in Table 1. Velocity data were missing in part of the observation period at the third depth at site M3 and the second depth at M6. The missing part at these sites was filled with velocity data obtained at the second depth at the same site for M3 and by linear

interpolation in the vertical direction for M6. Hence, the length of the velocity data became 350 to 400 days.

The velocity data were filtered with a tide eliminating filter (Thompson, 1983) and subsampled at 12-hour intervals. Then we obtained a cross-spectrum matrix that consists of cross-spectra for all possible combinations of velocity, after dividing the velocity data into about 12 overlapping segments whose length is 64 days, removing the mean value, and applying the Hanning filter. To increase statistical confidence four adjacent frequencies were grouped into a band and cross-spectra were averaged in each band. Thus cross-spectra were averaged for both segments and frequency bands. Mean values of averaged frequencies were 0.039, 0.10, 0.16, and 0.23 cpd for the lowest four frequency bands, corresponding to periods of 64-16, 12.8-8, 7.1-5.3, and 4.9-4 days, respectively. In this study, these four frequencies are referred to as subtidal frequencies and the motion at these frequencies is examined. From the cross-spectrum matrix we obtained eigenvectors, which correspond to EOFs, and eigenvalues, which correspond to the variability explained by EOFs, for each frequency. The interval in which velocity data were obtained differed slightly between sites (Table 1). To use as much data as possible, cross-spectra between two velocities were calculated in the entire period in which both velocities were obtained. Thus the period used to calculate cross-spectra was slightly different for each velocity pair. Cross-spectra and EOFs were also calculated only for the common interval in which all velocities were obtained but the EOFs depend little on the change of the interval.

Since the spatial distribution of velocity data is not uniform, velocity data were weighted when cross-spectra were calculated. The weight was defined so that the sum of the variance of the weighted velocity becomes the total kinetic energy integrated in the two vertical cross sectional areas along 49.5N and 53N. To do this, these cross sectional areas were divided into segments by using vertical and horizontal lines that are in the middle of two adjacent sites and nominal depths in Table 1, respectively. Since the integral of kinetic energy can be approximated by the sum of the velocity variance in each segment multiplied by the area of the segment, the velocity weight was defined as the square root of the segment area. The value of the area is listed in the last column in Table 1. Then the orthogonality condition for EOFs of weighted velocity indicates that the EOFs are energetically independent of each other and, hence, the total kinetic energy is expressed as the sum of the variance of each EOF.

3. Results

a. Structure of variability

As an example of the filtered velocity data, stick plots of velocity observed at site M2 are examined (Fig. 2). Subtidal and seasonal variability existed in the ESC. This subtidal variability was visually correlated in the vertical direction with its amplitudes at the two depths similar to each other. The power spectral density of along-isobath velocity at all mooring sites basically decreased monotonically with frequency at most sites without any

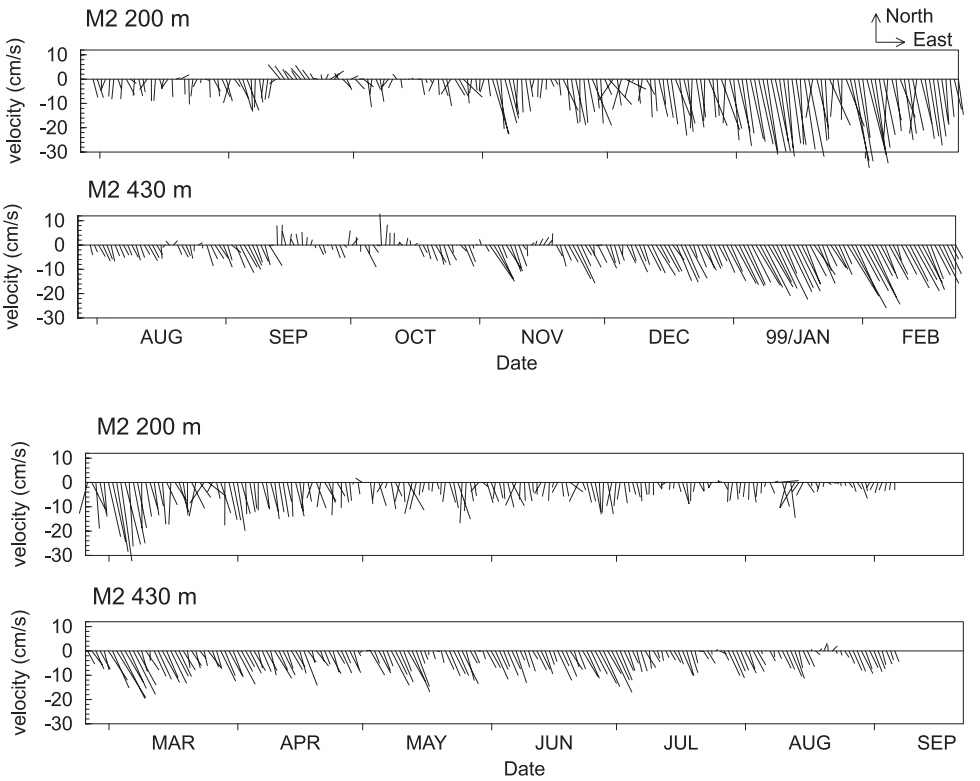

Figure 2. Stick plots of filtered velocity observed at mooring site M2 at depths of 200 m and 430 m. A velocity stick is drawn for each day.

significant peaks (Fig. 3). The power spectral density at sites M1 and M5, located over the shelf, was higher than that at the other sites at all frequencies. The power spectral density was almost uniform with depth at sites M2 and M3 at frequencies lower than 0.15 cpd, whereas the power spectral density was slightly higher at the second depth than the other depths at higher frequencies. At sites M4 and M6, the power spectral density was higher at the shallowest depth than at the other depths. The total kinetic energy of motion at subtidal frequencies corresponded to about 40% of that at tidal frequencies and is not small.

About 50%, 15–20%, and 10–15% of total kinetic energy at frequencies lower than 0.48 cpd are explained by the first, second, and third EOFs, respectively (Fig. 4). The coherence between the first EOF and along-isobath velocity is high at sites M1 and M5 which are located over the shelf (Fig. 5a). It is not surprising that the coherence between the first EOF and along-isobath velocity is higher at M5 than M1, since the weight of velocity at M5 is about two times larger than that at M1 (Table 1). The coherence between the second EOF and along-isobath velocity is generally low over the shelf and high at sites M2, M3, and M6 which are located over the slope and M4 which is located in the rather flat

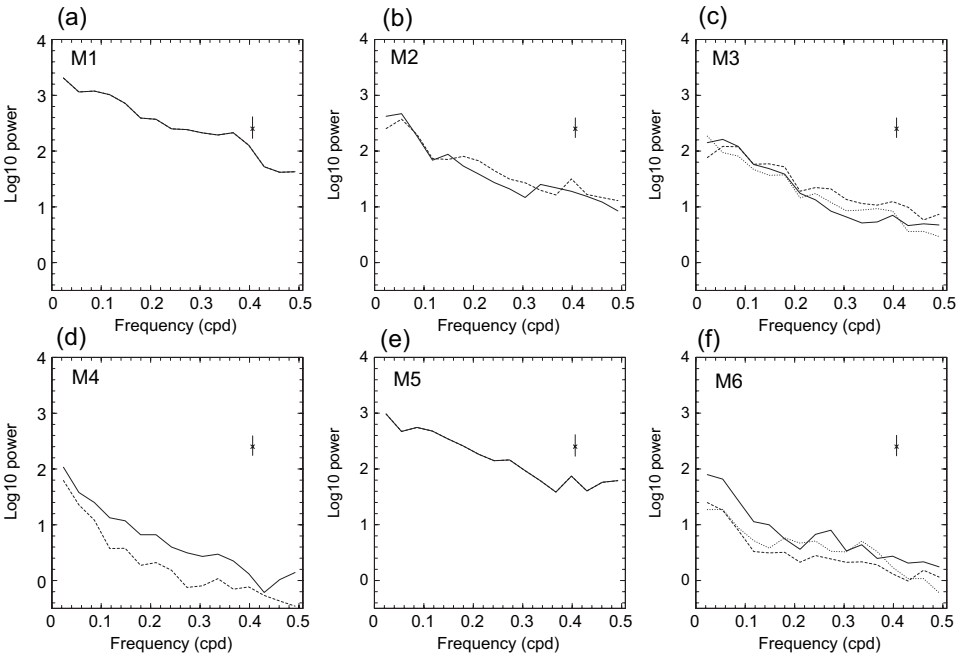

Figure 3. The power spectral density ($cm^2\ s^{-2}\ cpd^{-1}$) of along-isobath velocity at the first (solid lines), second (dashed lines), and the third (dotted lines) depths at mooring sites M1–6 versus frequency (cpd). The vertical axis is on a logarithmic scale. The vertical bars with the crosses indicate the 95% confidence interval.

region offshore (Fig. 5b). The variance ellipse of the first EOF is large over the shelf and linearly polarized with the major axis of the ellipse almost parallel to the isobath (Fig. 6a). The variance ellipse of the second EOF is large over the slope at 53N except at a frequency of 0.23 cpd (Fig. 6b). The variance ellipse is again linearly polarized. The major axis of the ellipse is generally parallel to the isobath over the slope, while across-isobath motion is evident especially at site M4 at the lowest frequency. Therefore, the first and second EOFs represent the motion confined over the shelf and slope, respectively, corresponding to the variability of the two cores of the intense flow of the ESC (Ohshima *et al.,* 2002; Mizuta *et al.,* 2003). The vertical change of the motion is less significant at most sites for both the first and second EOFs.

The phase relationship of velocity at different sites is shown in Figure 6. The real part of the velocity shown by bars corresponds to velocity that is in phase with the EOFs. For the sake of the later analysis the phase of along-isobath velocity for the first and second EOFs was set to zero at sites M1 and M2, respectively, since the motion by the EOFs is typically represented by along-isobath velocity at these sites. Thus along-isobath velocities at these sites were made real and in phase with the EOFs.

The relative importance of the lowest three EOFs for the variability over the shelf and

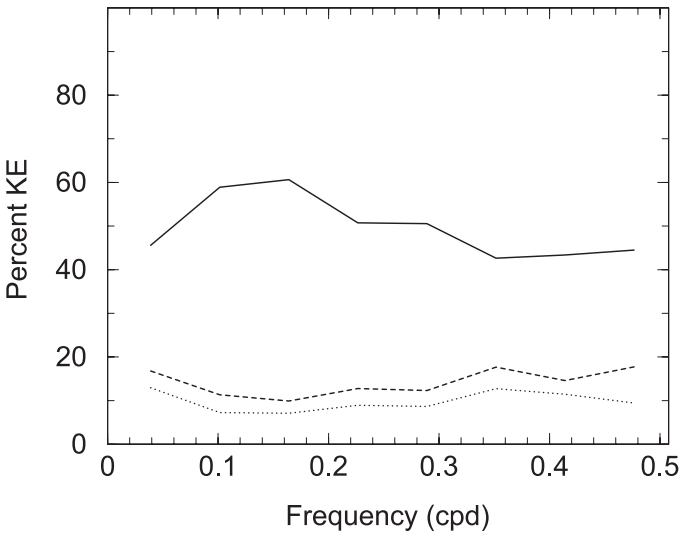

Figure 4. Percentages of the total kinetic energy explained by the first (solid line), second (dashed line), and third (dotted line) EOFs versus frequency.

slope are examined, by using percentages of kinetic energy at sites M1 and M2 (Fig. 7). More than 50% of kinetic energy at site M1 is explained by the first EOF which represents the motion confined over the shelf at frequencies lower than 0.35 cpd. At higher frequencies, the first EOF is confined to site M5 (not shown) and the percentage of kinetic energy at site M1 becomes small. Except for frequencies between 0.28 and 0.35 cpd, the

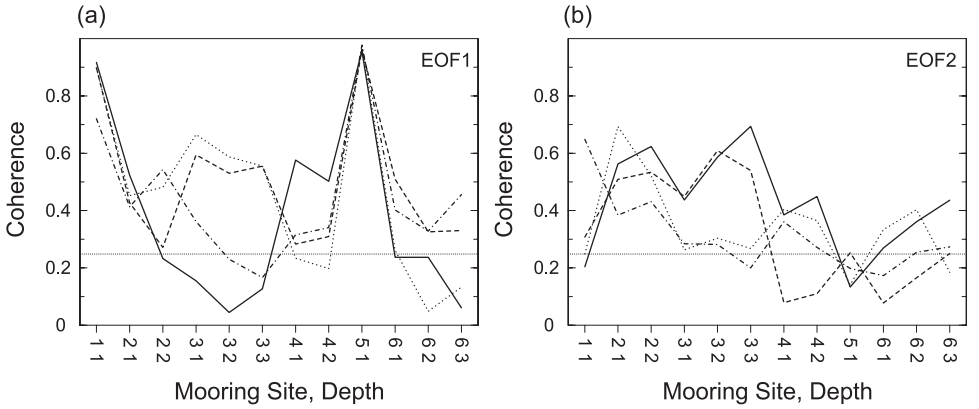

Figure 5. Coherence between along-isobath velocity and (a) the first EOF and (b) the second EOF at frequencies of 0.039 (solid lines), 0.10 (dashed lines), 0.16 (dotted lines), and 0.23 cpd (dash-dotted lines). The first and second digits of numbers for the horizontal axis denote the number of mooring site and depth, respectively. The dotted horizontal lines indicate the 95% confidence limit.

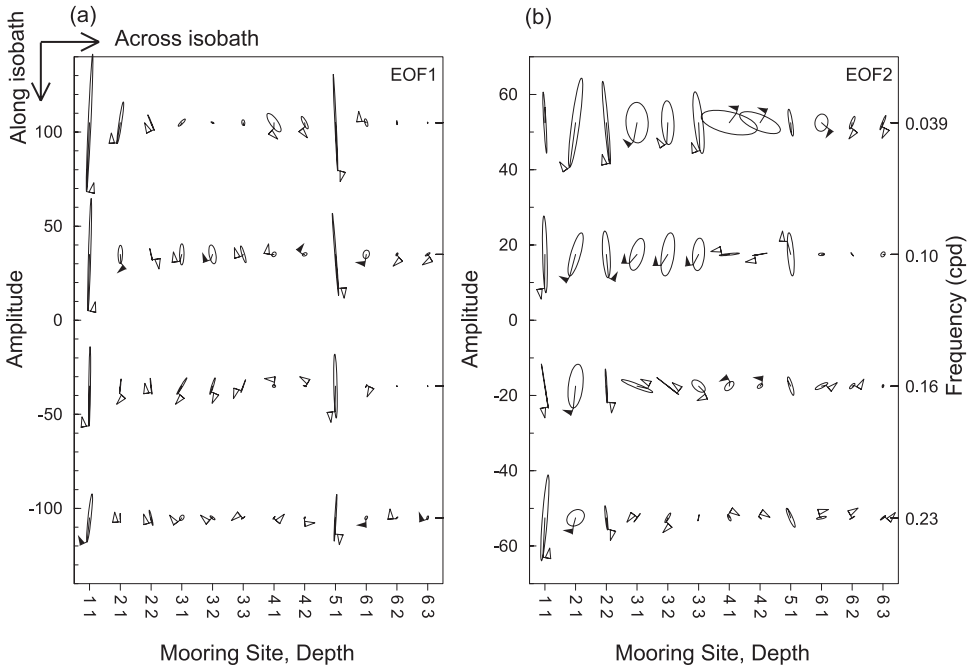

Figure 6. Variance ellipses of velocity (cm s^{-1} cpd^{-1}) of (a) the first EOF and (b) the second EOF at frequencies of 0.039 (upper ellipses), 0.10 (upper middle ellipses), 0.16 (lower middle ellipses), and 0.23 cpd (lower ellipses). The first and second digits of numbers for the horizontal axis denote the number of mooring site and depth, respectively. The arrows and bars headed by them for each ellipse indicate the direction of rotation and the real (in phase) part of velocity, respectively. Here the solid, open, and no arrows are drawn when the coherence between the EOF and the velocity along both the major and minor axes, only the major axis, and none of the axes exceeds 95% confidence limit, respectively. See the text for the definition of the real part of velocity.

largest part of kinetic energy at site M2 is explained by the second EOF which has large amplitude over the slope. Thus, the second EOF is important for the variability over the slope.

b. Comparison with a CTW model

The phase difference between along-isobath velocities of the first EOF at sites M1 and M5, where the motion represented by the first EOF is large, is compared with the phase difference calculated from a CTW model (Brink and Chapman, 1987) in Figure 8a. The profile of density and bottom topography used in the model were determined from CTD measurements and the bottom depth measured at CTD stations around the mooring sites, respectively. The model did not include variation of density profile and bottom topography in the along-isobath direction, a mean flow in the background, nor modification of the structure and propagation speed of CTWs by dissipation. The phase of the first EOF at site

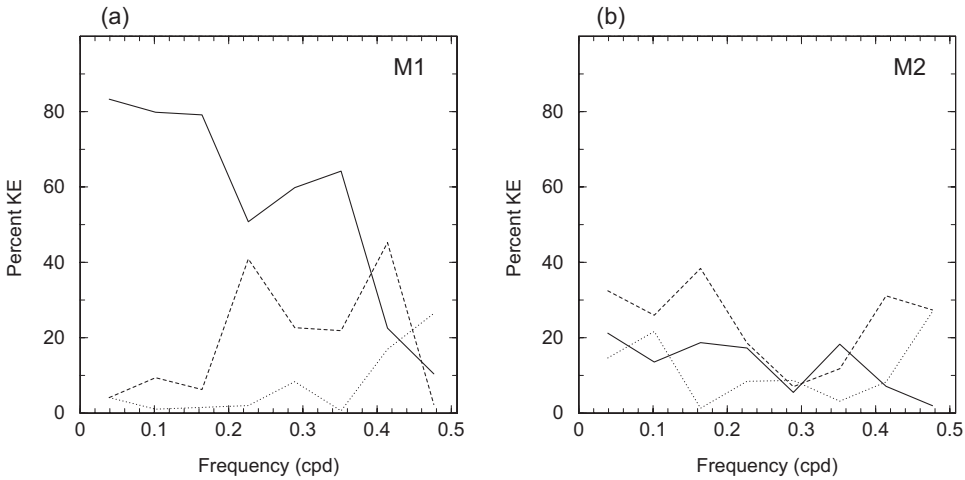

Figure 7. Percentages of kinetic energy at mooring sites (a) M1 and (b) M2 explained by the first EOF (solid line), second EOF (dashed line), and the third EOF (dotted line) versus frequency. Vertically averaged kinetic energy was used for site M2.

M5 is smaller than that at M1 for all frequencies, indicating that the phase of the first EOF propagates from M1 to M5 (Fig. 8a). At the lowest three frequencies the phase difference of the first EOF coincides with that of the free, first-mode CTW calculated with bottom

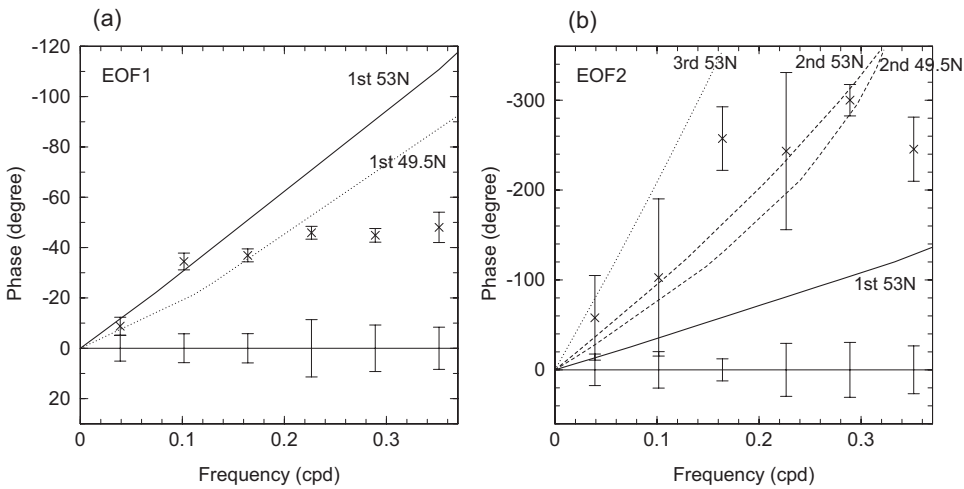

Figure 8. (a) The phase difference between along-isobath velocities at sites M1 and M5 for the first EOF (crosses) and the first-mode CTWs versus frequency. (b) The phase difference between along-isobath velocities at sites M2 and M6 for the second EOF (crosses) and the lowest three modes of CTWs versus frequency. The vertical bars on horizontal lines indicate the 95% confidence limit of the phase at M1 and M2 in (a) and (b), respectively. The vertical bars at crosses indicate the 95% confidence limit of the phase at M5 and M6 in (a) and (b), respectively.

topography at 53N (solid line) and 49.5N (dotted line). At higher frequencies the former is smaller than the latter, suggesting the effects of forced motion. The phase difference between along-isobath velocities of the second EOF at sites M2 and M6 is compared with the phase difference for free CTWs (Fig. 8b). The phase difference of the second EOF contains larger errors than that of the first EOF. Nevertheless, the phase difference for the second EOF lies between those calculated from the first- and third-mode CTWs (solid and dotted lines, respectively) and roughly close to the phase difference of the second-mode CTW calculated with bottom topography at 53N (dashed line) and 49.5N (thin dashed line).

The phase speeds of the first- and second-mode CTWs are 5.4–8.5 and 2–2.5 m s^{-1}, respectively. Since these phase speeds are larger than the speed of the ESC which attains a maximum of 0.37 $\pm$ 0.09 m s^{-1} in January (Mizuta *et al.,* 2003), advection by the ESC is expected to be negligible for these waves to the first approximation. Effects of the seasonal change of stratification on properties of CTWs are also examined, using strong stratification observed in fall and weak stratification in winter. Stratification was determined in winter by assuming that stratification observed in fall is weakened by mixing down to a depth of 150 m, since cold water that is a remnant of a winter mixed layer is found at depths of 100–150 m. The change of the phase speed of CTWs with these variations in stratification is less than 10% and thus negligible to the first approximation.

Variance ellipses of CTWs at each mooring site are examined (Fig. 9), where the amplitudes of CTWs were normalized with the alongshore component of the kinetic energy flux at both 53N and 49.5N (Brink, 1989). The motion of the first-mode CTW is confined to sites M1 and M5 and strongly polarized with the major axis of the ellipse parallel to the isobath. These features are also found for the first EOF (Fig. 6a). Thus the first EOF can be explained by the first-mode CTW. The amplitude of the second-mode CTW is large at site M2 at 53N which is located near a maximum of along-isobath velocity of this CTW. The variance ellipse is linearly polarized with the major axis parallel to the isobath there. These features are also found for the second EOF (Fig. 6b). On the other hand, there are some differences between the second-mode CTW and second EOF. That is, strong across-isobath motion is found at site M4 at a frequency of 0.039 cpd for the second EOF (Fig. 6b), while such motion is not found for the second-mode CTW. The motion by the second EOF at site M1 is larger and in phase with that at M2 at higher frequencies. A large variance ellipse is obtained at site M5, which is closer to the coast than the other sites, for the second-mode CTW (Fig. 9b), and the ratio of the motions at M5 and M6 (not shown) for the second-mode CTW is larger than that for the second EOF. These features indicates that the second EOF cannot be reproduced only by the inviscid, second-mode CTW but they are expressed as a mixture of second and other modes of CTWs.

c. Relationship between the first EOF and wind stress

To clarify the driving mechanism of the motion represented by the EOFs, we examine the relationship between the EOFs and the wind stress, (τ^x, τ^y), where superscripts x and y

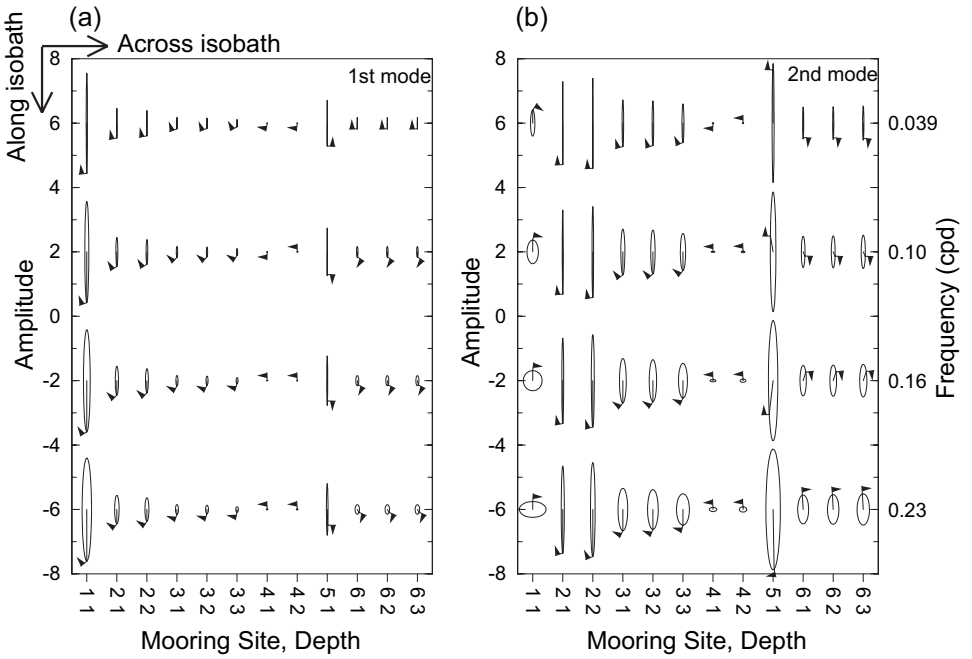

Figure 9. The same as Figure 6 except for variance ellipses of (a) the first-mode CTW and (b) the second-mode CTW. The vertical axis is scaled by 10^{-7}.

indicate the eastward and northward components, respectively. The wind stress was obtained from 10-m winds of the European Centre for Medium-Range Weather Forecasts reanalysis data (ERA-40) with Gaussian (N80) grid and a drag coefficient reduced to neutral stability by Large and Pond (1981). Although the Sea of Okhotsk is a seasonal ice zone, the change of the drag coefficient by sea ice was neglected for simplicity. Then cross-spectra between the EOFs and each component of the wind stress were calculated at each grid point of the ERA-40. Divided by the amplitude of the EOF, the cross-spectra represent the spectra of the wind stress correlated with the EOF. The coherence and phase between the EOFs and τ^x and τ^y were also calculated from the cross-spectra.

The wind stress correlated with the first EOF is expressed by variance ellipses in Figure 10. The coherence between the EOF and wind stress, τ^L, parallel to the major axis of the variance ellipse is also indicated by contours. Note that the direction of τ^L changes in space and with frequency. Except for a frequency of 0.23 cpd, the wind stress which is correlated with the first EOF is large over the northern and western shelves. The wind stress is polarized with the major axis nearly parallel to the coast in those regions. The 95% confidence limit of the coherence between EOFs and τ^L is 0.27. The coherence is significant in most parts of the Sea of Okhotsk, with large values occurring over the shelf where variance ellipses are large.

The direction of τ^L and the phase relationship between the first EOF and τ^L are

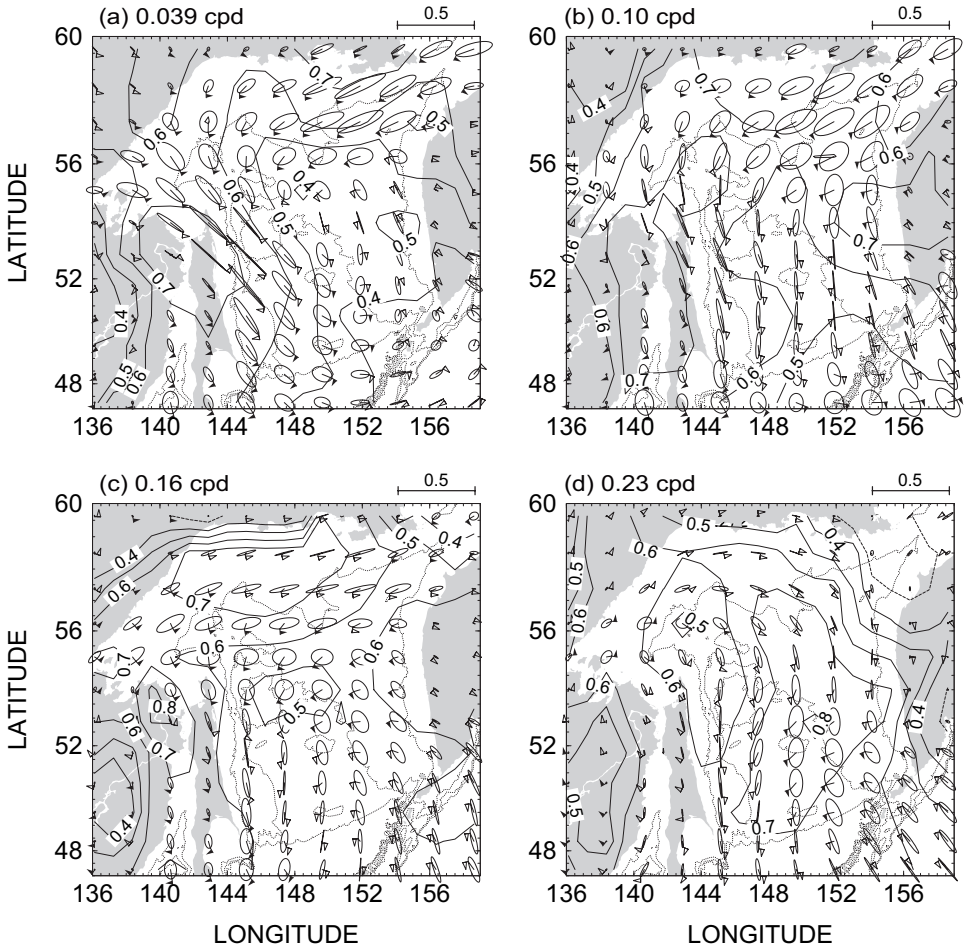

Figure 10. Variance ellipses of the wind stress correlated with the first EOF (N m^{-2} cpd^{-1}) at subtidal frequencies. As in Figure 9 the arrows and bars indicate the direction of rotation and real part of the wind stress, respectively. Contours indicate the coherence between the first EOF and the wind stress, τ^L, parallel to the major axis of the variance ellipse. The dashed lines indicate contours of the 95% confidence limit. The dotted lines show isobaths of 200, 1000, and 1500 m and the shading indicates land. Caribration vectors for the wind stress are shown at the top of each panel.

examined (Fig. 11). The real part of the flow at site M1 by the first EOF is almost parallel to the isobath and directed in the propagation direction of CTWs (see variance ellipses in Fig. 11). Thus the direction of τ^L over the northern and western shelves was chosen so that τ^L also has the along-isobath component oriented in the propagation direction of CTWs, by using the fact that τ^L can be rotated by 180° arbitrarily. The phase of τ^L leads that of the first EOF over the northern and northwestern shelves at all frequencies, except for a small delay over the northwestern shelf at a frequency of 0.039 cpd. The value of the phase

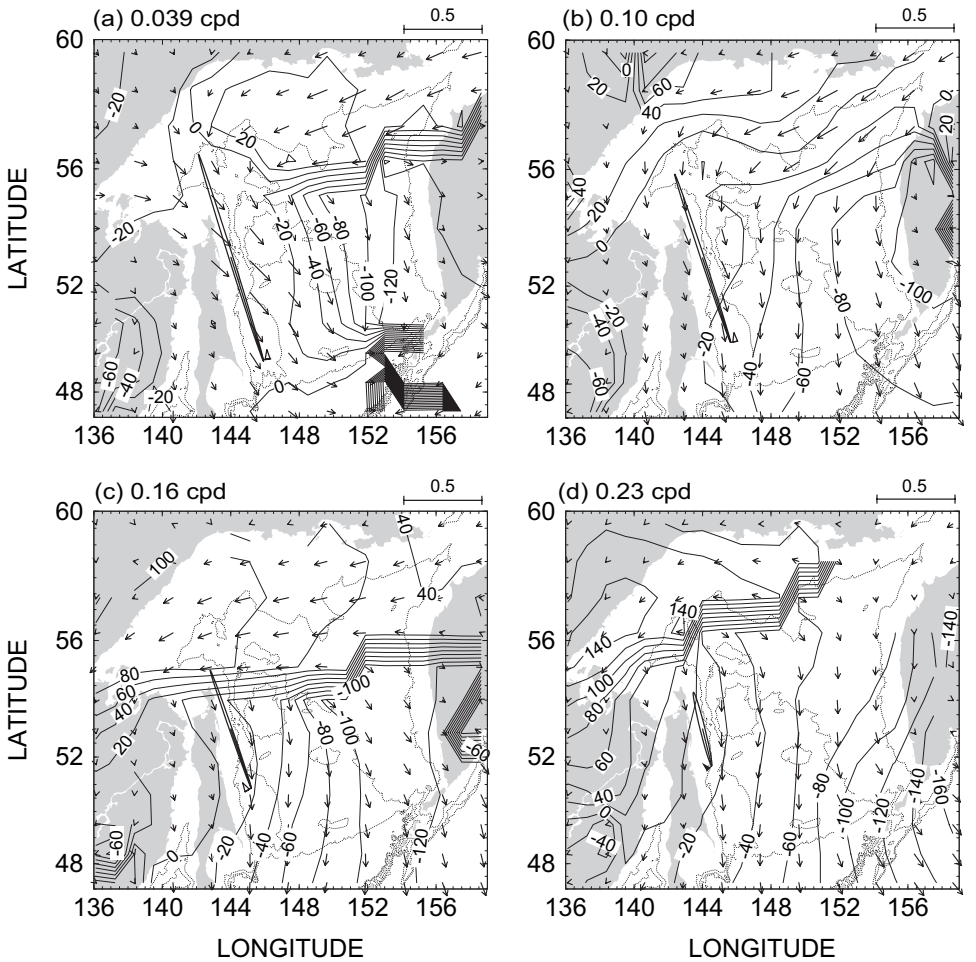

Figure 11. Wind stress vectors for τ^L (N m^{-2} cpd^{-1}) and contours of the phase between τ^L and the first EOF at subtidal frequencies. Contours are not drawn in the region where the error of the phase exceeds 45°. Also shown are variance ellipses of the first EOF velocity at site M1 (see Fig. 6a for details of these variance ellipses).

decreases in the propagation direction of the CTW along the northern and northwestern shelves and becomes nearly zero over the western shelf near site M1. The spatial change of the phase, θ, over the northwestern shelf increases with frequency, f. The mean phase speed, c, between two locations is expressed in terms of the phase difference, δθ, and the distance, δy, between these locations as $c = 2\pi f \delta y/\delta\theta$. The CTW is nondispersive when its wavelength is greater than the width of the shelf. This relationship between θ and f is qualitatively consistent with the dispersion relation of CTWs. Thus it is suggested that a

resonance between the CTW and the alongshore wind stress over the northern and northwestern shelves occurs to drive the motion represented by the first EOF.

The dispersion relation indicates that the wavelength of the free CTW and, hence, the scale of the wind stress that is resonant with the CTW decreases with frequency. On the other hand, to estimate the typical horizontal scale of the wind stress at each frequency, the coherence of the wind stress at two different points was calculated with varying the distance between the points. The e-folding scale of the coherence was 700–1000 km and changed little at the frequencies of the lowest four EOFs. Thus it is suggested that the amplitude of the wind stress that is resonant with the CTW changes with frequency. In fact the amplitude of τ^L decreases over the northern and northwestern shelves at higher frequencies (Fig. 11). At a frequency of 0.23 cpd τ^L is large mostly over the western shelf where the phase of τ^L is almost uniform in space (Fig. 11d). Note that the phase difference between 53N and 49.5N of the free, first-mode CTW is 50–70° at a frequency of 0.23 cpd (Fig. 8a). The spatial change of the phase of τ^L is smaller than this. The distribution of τ^L is more confined over the western shelf with its phase being uniform in space at frequencies higher than 0.23 cpd (not shown). This uniform phase of the wind stress can account for the discrepancy between the phase changes of the first EOF and free CTW (Fig. 8a), since the phase propagation of a wave excited by an uniform forcing is twice as fast as that of a free wave. That is, the amplitude, ϕ, of a CTW excited by a wind forcing, Y, is determined from

$$\phi_y - \frac{1}{c}\,\phi_t = Y, \tag{1}$$

where y is the distance along the coast, t is time, and c is the constant propagation speed of the CTW. If Y is applied uniformly in space in the area $y \geq 0$ and expressed as

$$Y = \begin{cases} 0 & \text{at } y < 0 \\ Ae^{-i\omega t} & \text{at } y \geq 0 \end{cases} \tag{2}$$

with a boundary condition being $\phi = 0$ at $y = 0$, then

$$\phi = \frac{2cA}{\omega} \sin\frac{\omega y}{2c}\, e^{(i\omega/2c)(y-2ct)}. \tag{3}$$

Thus the propagation speed of ϕ excited by the uniform wind stress is twice as large as that of the free CTW. This is consistent with the phase difference between the first EOF and the first-mode, free CTW (Fig. 8a) at higher frequencies.

d. Relation between the second EOF and wind stress

The coherence between the wind stress and second EOF is significant (Fig. 12). The coherence at a frequency of 0.16 cpd is smaller than that at the other frequencies but still exceeds the 95% confidence limit of 0.27 in some regions. The coherence with the second EOF is high in the central part of the basin whereas that with the first EOF is high over the shelf. The major axis of variance ellipses of the wind stress correlated with the second EOF

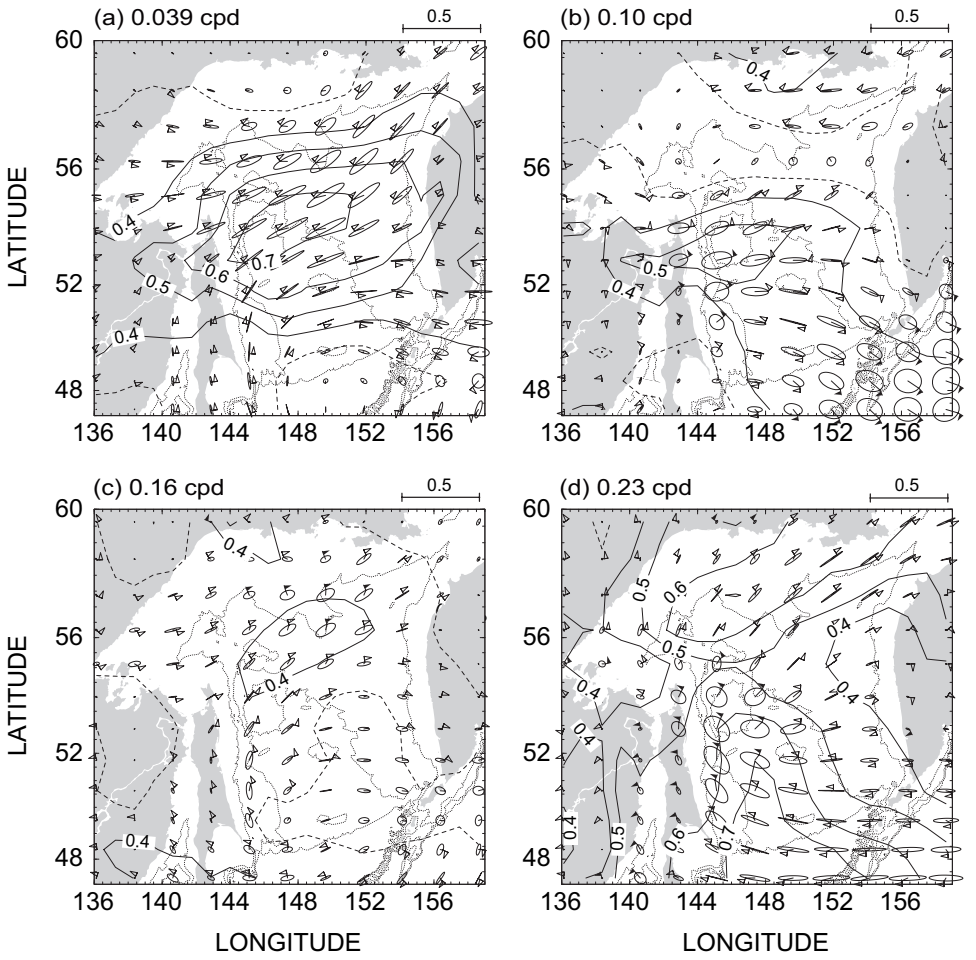

Figure 12. The same as Figure 10 except for the wind stress correlated with the second EOF (N m^{-2} cpd^{-1}).

is not necessarily parallel to the coast. Thus it is suggested that the driving mechanisms of the motion represented by the first and second EOFs are different.

The coherence between the wind stress curl at each grid point of ERA-40 and the second EOF is examined (Fig. 13). The coherence is high in the area where the curl of the wind stress shown in Figure 12 seems to be large. At all frequencies except for 0.16 cpd the coherence is most high in the central part of the basin. Large areas of high coherence are located over the northern shelf and in the central part of the basin at 0.039 cpd and over the eastern and northern slopes at 0.10 and 0.23 cpd. The continental slopes in the northern and eastern parts are broader than those in the western part. Except for the high coherence over the northern shelf at a frequency of 0.039 cpd, the high coherence regions noted above are

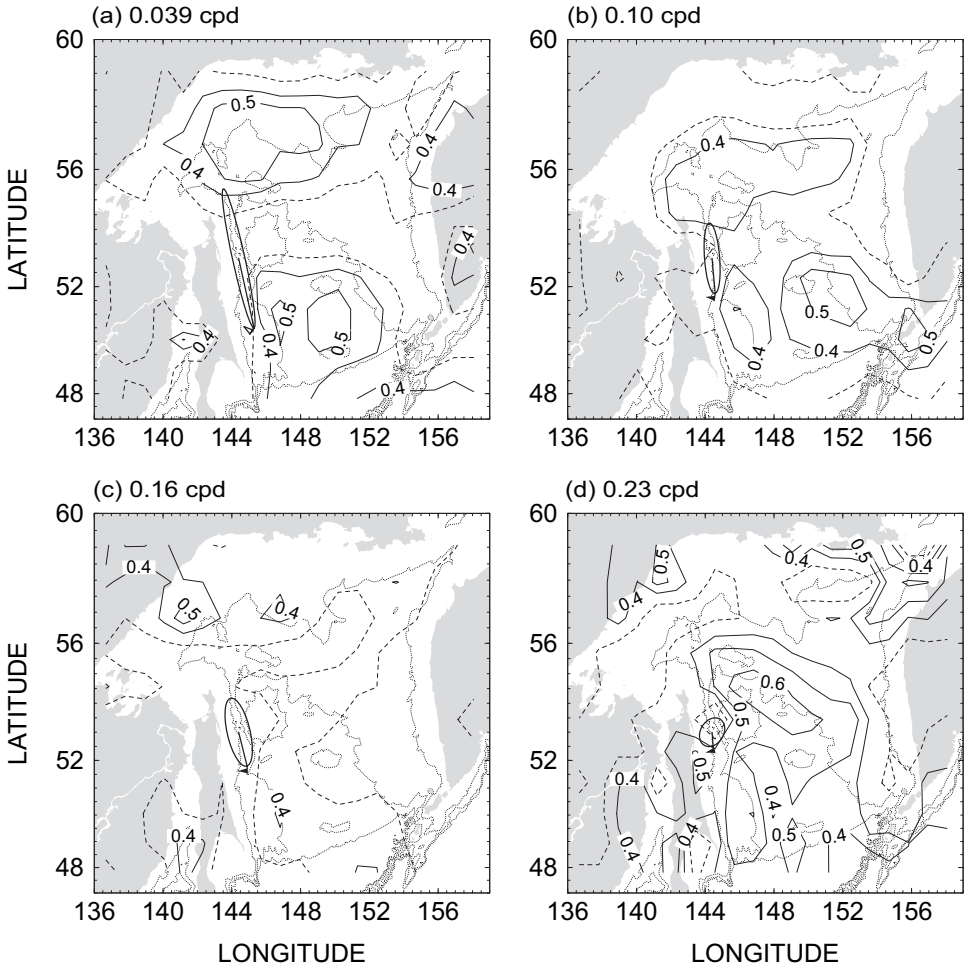

Figure 13. Contours of the coherence between the second EOF and the wind stress curl at subtidal frequencies. The dashed lines indicate contours of the 95% confidence limit. Also shown are variance ellipses of the second EOF velocity at the first depth of site M2 (see Fig. 6b for details of these variance ellipses).

located over or near the broad slopes in the northern and eastern parts. The circulation induced by the wind stress curl in these regions tends to be elongated along the isobath by the topographic beta effect. When the wind stress curl is positive, it tends to induce an elongated cyclonic circulation, causing an along-isobath flow in the propagation direction of a CTW near the coast. This direction of the flow relative to the isobath coincides with that of the real part of the flow at site M2 (see variance ellipses in Fig. 13). The phase relation between the wind stress curl and the second EOF will be discussed later.

At a frequency of 0.039 cpd the coherence is also high in a region over the northern shelf

(Fig. 13a). This high-coherence region disappears, when the second EOF is calculated without the velocity data at site M4. Other features of the distribution of the coherence depends little on this change of the second EOF at all frequencies. Thus the high-coherence region over the northern shelf found at a frequency of 0.039 cpd is related only to the variability of velocity at site M4 at this frequency (Fig. 6b).

Chapman and Brink (1987) numerically investigated the flow over the shelf and slope induced by a forcing in the deep, offshore region. They showed that the distribution of the flow changes drastically with the frequency of the forcing: the flow is confined over the slope due to bottom friction at frequencies lower than about 0.1 cpd, while the flow over the shelf increases at higher frequencies. As shown in Figure 6b the motion by the second EOF is strong over the slope at lower frequencies, while the motion is strong over the shelf at the highest frequency of 0.23 cpd. These features of the second EOF are consistent with the argument by Chapman and Brink (1987).

The phase relationship between the second EOF and the wind stress curl is examined from the phase of their cross-spectra (Fig. 14). In the central part of the basin the phase of the wind stress curl leads that of the second EOF at all frequencies. In the region where the coherence is higher than 0.4, the phase changes clearly in space at a frequency of 0.23 cpd, decreasing from south to north over the eastern slope and from east to west over the northern slope. At a frequency of 0.10 cpd the phase in the high coherence regions is $60-140°$ over the eastern slope and decreases to $-40-0°$ over the northern slope. This relatively large difference of the phase in the two regions appears to be related to the fact that the wind stress curl tends to take opposite signs between these two regions (Fig. 12b). The spatial change of the phase found at frequencies of 0.10 and 0.23 cpd suggests that the motion represented by the second EOF propagates along the isobath from the eastern and northern slopes to mooring sites. Note that even at a depth of 1000 m the topographic beta effect over the northern and eastern slopes is about 10 times stronger than the planetary beta effect.

In the following, the distribution of the phase is examined more precisely. For the wind stress correlated with the first EOF the spatial change of the phase of the wind stress increases with frequency, being consistent with the dispersion relation of long CTWs (Fig. 11). The spatial change of the phase is also found in the wind stress curl correlated with the second EOF at frequencies of 0.10 and 0.23 cpd (Fig. 14). However, the magnitude of the change of the phase decreases with frequency. The region of high coherence is smaller for the second EOF than that for the first EOF, indicating that the forcing region of the second EOF is smaller than that of the first EOF (Figs. 10 and 13). Hence, if the Fourier transformation in space is applied, the forcing to the second EOF in the wavenumber domain is distributed over a broader range of wavenumbers than that of the first EOF. The wavenumbers of the wind stress curl at subtidal frequencies are compared with dispersion curves of CTWs over the shelf and slope in the northern and eastern parts (Fig. 15). The ETOPO5 from the National Geophysical Data Center was used for bottom topography. Crosses in the figure indicate the wavenumbers, $l_f = \delta\theta/\delta y$, of the wind stress curl

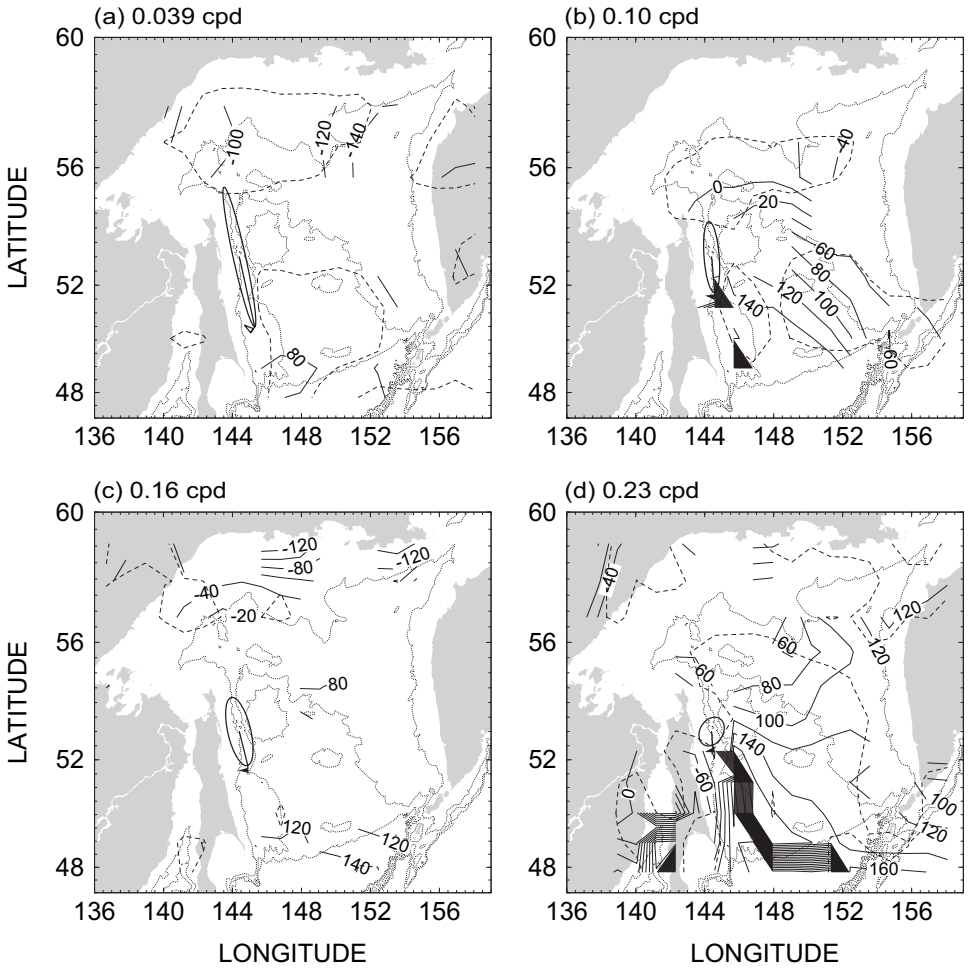

Figure 14. Contours of the phase between the wind stress curl and the second EOF at subtidal frequencies. Contours are not drawn in the region where the error of the phase exceeds 45°. The dashed lines indicate the region where the coherence was higher than 0.4. Also shown are variance ellipses of the second EOF velocity at the first depth of site M2.

determined from Figure 14, where δy is the distance along 1000-m isobath and $\delta\theta$ is the change of phase in δy. The l_f is close to the wavenumber of the third-mode CTW at 0.10 cpd and between the wavenumbers of the first- and second-mode CTWs at 0.23 cpd. Phase propagation is not clear at 0.039 cpd, indicating that $l_f \sim 0$ at this frequency. When the wind stress curl is limited to a region that has a horizontal scale of L, the wind stress curl in the frequency domain is extended typically within a scale of L^{-1} around l_f. Since L is estimated to be $\sim$300 km from the size of high coherence region in Figure 13, L^{-1} becomes $\sim 3 \times 10^{-6}\,\mathrm{m}^{-1}$ which is of the same order as l_f. Thus although the

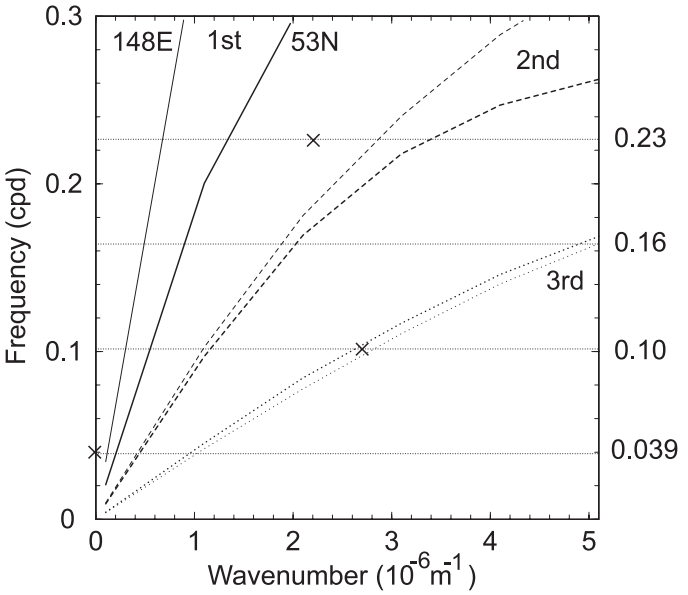

Figure 15. Dispersion curves of the lowest three modes of CTWs. The solid, dashed, and dotted lines indicate the dispersion curve of the first-, second-, and third-mode CTWs, respectively. The thick and thin lines indicate the dispersion curves calculated with bottom topography of the eastern slope around 53N and the northern slope at 148°E, respectively. The crosses denote the wavenumbers, l_f, of the forcing to the second EOF. The dotted horizontal lines indicate the four subtidal frequencies.

wavenumbers of the forcing are different from those resonant to a particular mode of CTW, the wavenumbers of the lowest two or three modes of CTWs exist within the wavenumbers of the forcing, $l_f \pm L^{-1}$, at all frequencies.

4. Summary and discussion

We investigated the variability of velocity in the ESC over the continental shelf and slope, focusing on the variability at the four subtidal frequencies of 0.039, 0.10, 0.16, and 0.23 cpd. By using the technique of empirical orthogonal functions in the frequency domain, the distribution of the amplitude and phase of the velocity variability at different sites and depths was examined at these four subtidal frequencies. The spectral power density of the velocity was larger over the shelf than over the slope and offshore region at all frequencies (Fig. 3). The first EOF represents this energetic motion over the shelf, having large amplitude and high coherence with the observed motion over the shelf (Figs. 5 and 6). The second EOF represents variability over the slope, having large amplitude and high coherence over the slope and explaining the largest part of kinetic energy there (Figs. 5, 6, and 7). The first and second EOFs, therefore, correspond to the variability of the two

cores of intense flow of the ESC over the shelf and slope described in Ohshima *et al.* (2002) and Mizuta *et al.* (2003). Variance ellipses of velocity are linearly polarized with the major axes being parallel to the isobath, especially at sites where variability is large for both EOFs (Fig. 6). The vertical structure of the EOFs is nearly barotropic.

The phase of the first EOF clearly propagates along the shelf in the propagation direction of CTWs (Fig. 8). The phase change and valiance ellipses of the first EOF coincide with those of the free, first-mode CTW calculated with realistic stratification and bottom topography, except that the phase change of the former is smaller than that of the latter at high frequencies (Figs. 6, 8, and 9). Thus the first EOF corresponds to the first-mode CTW. The phase change and variance ellipses of the second EOF are similar to those of the second-mode CTW, while some features of the second EOF over the shelf and offshore region suggest that other modes of CTWs also influence the second EOF (Figs. 6, 8, and 9).

The distribution of the cross-spectra between the EOFs and the wind stress over the whole area of the Sea of Okhotsk was examined (Figs. 10–14). The distribution of the cross-spectra allowed us to identify the region where the wind stress excites the motion represented by each EOF and the phase relation between the wind stress and the EOF at each frequency. The first EOF is highly correlated with the alongshore component of the wind stress over the northern and western shelves (Fig. 10). It is suggested that a resonance between the CTW and the alongshore wind stress occurs to drive the motion represented by the first EOF at lower frequencies (Figs. 10 and 11). At higher frequencies it is suggested that the first EOF corresponds to the first-mode CTW excited by the uniform wind stress. Such a CTW propagates at a speed twice as high as that of a free CTW, with being consistent with the higher propagation speed of the first EOF at higher frequencies (Fig. 8).

The second EOF is not correlated with the alongshore component of the wind stress (Fig. 12) but correlated with the wind stress curl in the central part of the basin (Fig. 13). The motion over the shelf represented by the second EOF increases with frequency (Fig. 6). This feature of the motion is consistent with the results of the numerical experiment by Chapman and Brink (1987) who studied a flow over the shelf and slope induced by an offshore forcing. The wind stress curl correlated with the second EOF leads the second EOF and tends to induce an along-isobath flow that is in the same sense as the flow of the second EOF at site M2 near the coast (Fig. 14). At some frequencies the phase changes clearly in space, suggesting that the motion represented by the second EOF propagates along the isobath from the eastern and northern slopes to mooring sites with the shallower side to the right. The wind stress curl contains the wavenumbers resonant to the lowest two or three modes of CTWs at each frequency, because the wind stress curl was limited to a rather small area.

The amplitude of the first and second EOFs changes seasonally and has a maximum in winter, consistent with strong winds in winter (not shown). However, the seasonal variability of the structure of the EOFs or the wind stress correlated with the EOFs was not clear presumably due to the limited period of data. This study has focused on the variability of currents at 53N and 49.5N off the east coast of Sakhalin Island, where two cores of

intense flow of the ESC are clear. The variability at higher latitudes where another core of the ESC associated with dense shelf water is clear (Mizuta *et al.,* 2003) has not been fully studied. These problems are left for future works.

Acknowledgments. The authors thank Nelson Hogg of Woods Hole Oceanographic Institution for helpful discussions and for providing the technique of empirical orthogonal functions in the frequency domain. Discussions with Ken Brink and David Chapman was also helpful. This work was supported by Core Research for Evolutional Science and Technology of Japan Science and Technology Corporation.

REFERENCES

Brink, K. H. 1982. A comparison of long coastal trapped wave theory with observations off Peru. J. Phys. Oceanogr., *12,* 897–913.

——1989. Energy conservation in coastal-trapped wave calculations. J. Phys. Oceanogr., *13,* 1011–1016.

Brink, K. H. and D. C. Chapman. 1987. Programs for computing properties of coastal-trapped waves and wind-driven motions over the continental shelf and slope. Technical Report WHOI-87-24, 2nd Edition, Woods Hole Oceanographic Institution, 119 pp.

Chapman, D. C. and K. H. Brink. 1987. Shelf and slope circulation induced by fluctuating offshore forcing. J. Geophys. Res., *11,* 11741–11759.

Gladyshev, S., L. Talley, G. Kantakov, G. Khen and M. Wakatsuchi. 2003. Distribution, formation and seasonal variability of Okhotsk Sea Mode Water. J. Geophys. Res., *108,* doi:10.1029/2001JC000877.

Kimura, N. and M. Wakatsuchi. 2000. Relationship between sea-ice motion and geostrophic wind in the Northern Hemisphere. Geophys. Res. Lett., *27,* 3735–3738.

Kitani, K. 1973. An oceanographic study of the Okhotsk Sea: particularly in regard to cold waters. Bull. Far Sea Fish. Res. Lab., *9,* 45–77.

Large, W. G. and S. Pond. 1981. Open ocean momentum flux measurements in moderate to strong winds. J. Phys. Oceanogr., *11,* 324–336.

Leonov, A. K. 1960. The Sea of Okhotsk. NTIS AD 639 585, National Technical Information Service, Springfield, VA, 95 pp.

Mizuta, G., Y. Fukamachi, K. I. Ohshima and M. Wakatsuchi. 2003. Structure and seasonal variability of the East Sakhalin Current. J. Phys. Oceanogr., *33,* 2430–2445.

Moroshkin, K. V. 1966. Water masses of the Sea of Okhotsk. U.S. Dept. of Commerce Joint Publication Research Service, 43942, 98 pp.

Ohshima, K. I., D. Simizu, M. Itoh, G. Mizuta, Y. Fukamachi, S. C. Riser and M. Wakatsuchi. 2004. Sverdrup balance and the cyclonic gyre in the Sea of Okhotsk. J. Phys. Oceanogr., *34,* 513–525.

Ohshima, K. I., M. Wakatsuchi, Y. Fukamachi and G. Mizuta. 2002. Near-surface circulation and tidal currents of the Okhotsk Sea observed with the satellite-tracked drifters. J. Geophys. Res., *107,* doi:10.1029/2001JC001005.

Parkinson, C. L. and A. J. Gratz. 1983. On the seasonal sea ice cover of the Sea of Okhotsk. J. Geophys. Res., *88,* 2793–2802.

Simizu, D. 2003. Numerical studies on the circulation of the Sea of Okhotsk, Ph.D. dissertation, Hokkaido University, 50 pp.

Simizu, D. and K. I. Ohshima. 2002. Barotropic response of the Sea of Okhotsk to wind forcing. J. Oceanogr., *58,* 851–860.

Talley, L. D. 1991. An Okhotsk Sea water anomaly: implications for ventilation in the North Pacific. Deep-Sea Res., *38,* (Suppl. 1), 171–190.

Thompson, R. O. R. Y. 1983. Low-pass filters to suppress inertial and tidal frequencies. J. Phys. Oceanogr., *13,* 1077–1083.

Wallace, J. M. and R. F. Dickinson. 1972. Empirical orthogonal representation of time series in the frequency domain. Part I: Theoretical considerations. J. Appl. Meteor., *11,* 887–892.

Yasuda, I. 1997. The origin of the North Pacific Intermediate Water. J. Geophys. Res., *102,* 893–909.

Received: *15 February, 2005;* revised: *15 August, 2005.*